Materials Advances

PAPER

View Article Online
View Journal | View Issue

Cite this: *Mater. Adv.*, 2025, 6, 5633

Synergistic bifunctional conjugated microporous polymer as an organic anode containing tetraphenylethene and thianthrene-5,5′,10,10′-tetraoxide units for lithium and sodium-ion batteries†

Bhargabi Halder,‡[a] Mohamed Gamal Mohamed, ‡*[bc] Kannadasan Kalidoss,[a] Ahmed A. K. Mohammed,[c] Poonam Nagendra Singh,[b] Tapomay Mondal,[b] Yunsheng Ye, [b] Perumal Elumalai *[a] and Shiao-Wei Kuo *[bd]

This study reports the synthesis and an early exploration of the electrochemical investigation of a donor–π–acceptor (D–π–A) conjugated microporous polymer (CMP), **TPEHBZ-ThBS**, incorporating tetraphenylethene and thianthrene-5,5′,10,10′-tetraoxide units for reversible Li^+/Na^+ storage. Potentially scalable and sustainable **TPEHBZ-ThBS CMP** is synthesized *via* Suzuki coupling of 2,8-dibromothianthrene-5,5′,10,10′-tetraoxide (**ThBS-Br$_2$**), 1,1,2,2-tetrakis(4-bromophenyl)ethene (**TPEH-Br$_4$**), and 1,4-phenylenediboronic acid, and its structure is confirmed through comprehensive characterization. Electrochemical testing in CR-2032 coin cells reveals discharge capacities of 410 mAh g^{-1} (LIB) and 260 mAh g^{-1} (SIB) at 0.1C. Additionally, the lithium-ion full cell using NMC811 as the cathode and **TPEHBZ-ThBS CMP** as the anode exhibits a discharge capacity of 122 mAh g^{-1} at 0.1C-rate. Dunn's method and power-law analysis indicate a hybrid charge storage mechanism, dominated by diffusion-controlled processes. The sulfonyl groups facilitate strong Li^+/Na^+ binding, promoting efficient charge transport. The high redox activity, stable structure, and fully conjugated backbone collectively contribute to the capacity, rate performance, and cycling stability of the CMP, underscoring its potential for advanced energy storage applications.

Received 19th June 2025,
Accepted 29th June 2025

DOI: 10.1039/d5ma00654f

rsc.li/materials-advances

Introduction

The growing concern over environmentally hazardous resource usage and pronounced energy demands has underscored the importance of developing efficient and sustainable energy storage solutions.[1–4] Devices for electrochemical energy storage, such as rechargeable batteries and supercapacitors (SCs) can store energy from both traditional and renewable energy sources, including solar, wind, water, and waste heat energy.[5–11] Among these, rechargeable LIBs have become widely recognized for their exceptional energy density, extended cycle lifespan, and relatively lower environmental impacts.[12–15] However, the commercial reliance on LIBs is increasingly scrutinized due to the limited global lithium reserves, which constitute just 0.0065% of the Earth's crust. This scarcity has driven researchers to explore alternative post-LIB chemistries, such as calcium-ion (CIB), magnesium-ion (MIB), and potassium-ion batteries (KIB),[16,17] and in particular, sodium-ion batteries (SIBs) stand out as an attractive choice to replace LIBs because of sodium's high abundance, accounting for 2.8% of the Earth's crust, and its intercalation chemistry, which closely resembles that of lithium. Despite these advantages, SIBs face challenges such as lower cell voltage and the need for larger, heavier electrodes, which limit their energy density and make them less suitable for portable dynamic applications. Consequently, SIBs are primarily explored for fixed and grid-scale energy storage applications.[18] One of the significant hurdles in SIB development is the anode material. Graphite, the standard anode material for LIBs, is unsuitable for SIBs due to its inability to intercalate the larger sodium ions

---

[a] *Electrochemical Energy Storage Lab, Department of Green Energy Technology, Madanjeet School of Green Energy Technologies, Pondicherry University, Puducherry, 605014, India. E-mail: drperumalelumalai@pondiuni.ac.in*

[b] *Department of Materials and Optoelectronic Science, Center for Functional Polymers and Supramolecular Materials, National Sun Yat-Sen University, Kaohsiung 804, Taiwan. E-mail: mgamal.eldin12@yahoo.com, kuosw@faculty.nsysu.edu.tw*

[c] *Department of Chemistry, Faculty of Science, Assiut University, Assiut 71515, Egypt*

[d] *Department of Medicinal and Applied Chemistry, Kaohsiung Medical University, Kaohsiung 807, Taiwan*

† Electronic supplementary information (ESI) available. See DOI: **https://doi.org/10.1039/d5ma00654f**

‡ These authors contributed equally.

(Na^+, 1.02 Å), resulting in structural deformation and poor reversibility. Moreover, graphite's use in fast-charging LIBs presents issues such as lithium dendrite formation on the electrode surface, leading to short circuits, rapid aging, and increased cell fading.[19,20] To overcome these limitations, researchers have investigated a variety of carbon-based materials as potential anode candidates for both LIBs and SIBs. These include carbons derived from biomass, conjugated microporous polymers (CMPs), metal–organic frameworks (MOFs), and those doped with various elements.[21] The development of high-capacity, highly reversible, rate-capable, and long-cycle-stable anode materials remains critical for advancing battery technology across all systems. CMPs have emerged as a promising class of multidimensional materials as organic electrodes in energy storage devices.[22–28] These materials are characterized by strong covalent bonds between their organic building blocks, making them highly attractive for advanced applications. Their ease of synthesis, large surface areas, excellent thermal stability, and low densities have contributed to their rising prominence in the field of electrode materials.[29–34] The CMPs offer unique advantages, including tunable molecular structures, cost-effectiveness, abundance, environmental compatibility, and high theoretical capacities, further establishing their potential in energy storage applications.[35,36] With a π-conjugated structure and distinct connecting groups, the CMPs demonstrate outstanding electrochemical performance, primarily due to the redox activity of their structural units. These properties make them suitable for diverse applications, such as photocatalysis, energy storage, gas separation, drug delivery, optoelectronics, nanofiltration, and water treatment.[37–44] Recent advancements in CMP research have concentrated on creating innovative materials synthesized through various chemical and electrochemical polymerization methods. CMP-based electrodes for LIBs and SIBs show significant improvement, highlighting their potential to revolutionize energy storage technologies[45,46] The inherent structural stability of these materials permits precise electronic modulation through heteroatom incorporation and the sulfonyl group (SO_2), enabling enhanced charge transport and electrochemical performance.[9,10] The introduction of donor–acceptor (D–A) architectures further facilitates bandgap engineering and lowers redox potentials *via* strong intramolecular electronic coupling, collectively leading to improved charge carrier mobility and elevated power density for high-performance electrochemical applications.[9,10] For instance, Wang *et al.* performed $FeCl_3$-catalyzed oxidative polymerization to create a thiophene-rich polymer of PTTE, which was used as an anode for LIBs and SIBs exhibiting a capacity of 973 and 370 mAh g^{-1} at 100 and 50 mA g^{-1}, respectively.[47] Similarly, Zhang *et al.* explored the Li^+ and Na^+ ion storage in the MOP-derived dicarbazyl and benzothiadiazole and employed them as an anode material, which delivered capacities of 99 mAh g^{-1} for Na^+ storage and 404 mAh g^{-1} for Li^+ storage at 100 mA g^{-1}.[48] Li *et al.* found that the extended π-conjugated systems are responsible for the enhanced charge transfer giving rise to increased ion diffusion along with producing a capacitive effect. The quick ionic diffusion is thought to be caused by the lamellar structure and micropores, as indicated by comprehensive studies.[49] Yang *et al.* constructed thiophene-rich polymer anodes for reversible Li^+/Na^+ storage, exhibiting 595 and 241 mAh g^{-1} capacities for LIBs and SIBs at 100 mA g^{-1}.[50] Mohamed *et al.* synthesized Py-A-CMP working as a cathode material in LIBs, which delivered discharge capacities of 196.6 mAh g^{-1}, respectively, at a rate of 0.1C.[51] TPEH and its derivatives have attracted a lot of recognition for their simple synthesis, versatile chemical modification, excellent thermal stability, and outstanding fluorescence quantum yields.[52] Thianthrene (Th) and its derivatives, such as ThBS, have been extensively explored for applications in photovoltaics, organic electronics, and catalysis. Their conjugated structures, sulfur, and SO_2 contents make them promising candidates for advanced energy storage electrodes, particularly in SCs and lithium-sulfur (Li–S) batteries.[53–55] In this study, a highly conjugated donor–π–acceptor (D–π–A) CMP, denoted as **TPEHBZ-ThBS CMP**, was successfully synthesized for use as an anode material in rechargeable LIBs and SIBs. **TPEHBZ-ThBS CMP** polymer was prepared *via* Suzuki coupling of **ThBS-Br$_2$** and **TPEH-Br$_4$**, employing $BZB(OH)_2$ as a linking agent. Detailed synthesis, structural, morphological, and spectroscopic analyses, along with the Li^+/Na^+ storage performances, were reported. In addition, mechanistic charge storage studies have also been reported through the power law and Dunn's method for the **TPEHBZ-ThBS CMP**. The key merits or unique advantages of this CMP over other carbonaceous anode materials lie in its sustainability, higher degree of conjugation, structural tunability, and potential for mass production, which make it a promising candidate for further optimization.

Experimental section

Materials

Zinc powder (Zn), and $Pd(PPh_3)_4$, glacial acetic acid (AcOH), *N*-methyl-2-pyrrolidone (NMP), titanium tetrachloride ($TiCl_4$), poly(vinylidene fluoride) (PVDF), hydrogen peroxide (H_2O_2), potassium carbonate (K_2CO_3), benzophenone (BZPH), thianthrene (Th), 1,4-phenylenediboronic acid [$BZB(OH)_2$], bromine solution (Br_2), and anhydrous magnesium sulfate ($MgSO_4$) were obtained from Acros and Sigma-Aldrich.

Preparation of TPEH-Br$_4$

BZPH (11 g, 60.13 mmol) and Zn (15.8 g, 241.63 mmol) were stirred in THF (350 mL) over an ice bath, followed by the dropwise addition of 13.2 mL of $TiCl_4$ and heating the solution for 48 h. Then, the reaction was quenched with 10% aqueous K_2CO_3 and extracted with EtOAc after solvent removal, yielding TPEH as a white crystalline solid [Scheme S1, ESI†]. Then, TPEH (6.7 g, 20.2 mmol) was dissolved in AcOH (75 mL) and DCM (150 mL) at 0 °C, and Br_2 solution (8.1 mL) was added. The reaction proceeded for 48 h at RT. After dilution with water and DCM extraction, the residue was washed with MeOH and recrystallized from DCM/MeOH to produce **TPEH-Br$_4$** as a white solid.[56,57] FTIR (KBr, Fig. S1, ESI†): 3057, 1474 cm^{-1}. ^1H NMR (Fig. S2, ESI†): 7.3 (8H), 6.9 (8H) ppm. ^{13}C NMR (Fig. S3, ESI†): 142.3–121.8.

Synthesis of ThBS-Br_2

Th (6 g, 0.027 mol) in AcOH (200 mL) and bromine (12 mL, 0.232 mol) were added with stirring at 80 °C for 24 h. Then, 30 mL of water was added to the mixture to precipitate the product. The solid was filtered and recrystallized from MeOH/DCM, yielding a white solid as Th-Br_2 [Scheme S2, ESI†]. Th-Br_2 (1.5 g, 0.004 mol) in AcOH (55 mL) was added dropwise to H_2O_2 (42 mL) under stirring for 24 h at 80 °C, and the precipitate was filtered and washed with water and $NaHCO_3$. The product was recrystallized from MeOH/DCM to obtain a **ThBS-Br_2** in the form of a white solid. FTIR (Fig. S4, ESI†): 3067, 1173 (sulfone group) cm^{-1}. ^1H NMR (Fig. S5, ESI†): 8.4–7.53 ppm.

Preparation of TPEHBZ-ThBS CMP

In a Schlenk flask, TPEH-Br_2 (3 mmol), **ThBS-Br_2** (3 mmol), and BZB$(OH)_2$ (9 mmol) were prepared under a nitrogen atmosphere following the Suzuki coupling procedure. To this mixture, 20 mL of water and 40 mL of DMF were added, and the temperature of the reaction mixture was 140 °C, with constant stirring for four days. The resulting green precipitate of **TPEHBZ-ThBS CMP** was washed with various organic solvents to remove impurities.

Results and discussion

Characterization of TPEHBZ-ThBS CMP

Fig. 1 shows the schematic of the synthesis of the key structural components, **TPEH-Br_4** and **ThBS-Br_2**, as depicted in Fig. 1(a) and (b). The preparation of **TPEH-Br_4** begins with the synthesis of TPEH, which is derived from the reaction of BZPH with Zn and $TiCl_4$. This initial step results in the formation of TPEH, which then undergoes bromination. The bromination reaction is carried out using a solution of Br_2 in a mixture of DCM and AcOH, yielding **TPEH-Br_4** as a white crystalline solid. To prepare **ThBS-Br_2**, the process begins with the reaction of the Th monomer with Br_2 in acetic acid. This step produces Th-Br_2, a white powder. The subsequent oxidation of Th-Br_4 is performed using H_2O_2 in AcOH. This oxidation step converts Th-Br_4 into ThBS-Br_4, which is also obtained as a white powder. The synthesis of **TPEHBZ-ThBS CMP**, illustrated in Fig. 1(c), involves a Suzuki coupling reaction. In this step, **TPEH-Br_4**, **ThBS-Br_2**, and BZB$(OH)_2$ are combined in a controlled environment. A coupling reaction is performed in a nitrogen atmosphere using a mixture of water and DMF. The reaction mixture is heated to 140 °C and stirred for four days. Upon completion of the reaction, the resulting green precipitate of **TPEHBZ-ThBS CMP** is collected. To confirm the structures of **TPEH-Br_4**, **ThBS-Br_2**, and **TPEHBZ-ThBS CMP**, FT-IR spectroscopy was employed, as shown in Fig. 2(a). The FT-IR spectra [Fig. 2(a)] reveal characteristic absorption bands at 3075, 3067, and 3029 cm^{-1}, corresponding to the stretching vibrations of aromatic C–H in **TPEH-Br_4**, **ThBS-Br_2**, and **TPEHBZ-ThBS CMP**, respectively. Additionally, prominent bands at 1173 and 1145 cm^{-1} are observed in **ThBS-Br_2**, and **TPEHBZ-ThBS CMP**, which are attributed to the presence of the SO_2 units in their structures.[55] The solid-state ^{13}C NMR spectrum of **TPEHBZ-ThBS CMP**, illustrated in Fig. 2(b), displays signals in the 112–103 ppm and 150–144 ppm regions, representing the two main types of carbon within the networks: aromatic carbons and $C{=}C$ bonds in the TPEH moiety.

Thermogravimetric analysis (TGA) was conducted on **TPEHBZ-ThBS CMP** under a nitrogen atmosphere in the temperature range of 40–800 °C [Fig. S6, ESI†]. The material exhibited only a 10% weight loss (T_{d10}) at 515 °C, highlighting its excellent thermal stability. At 800 °C, **TPEHBZ-ThBS CMP** demonstrated a high char yield of 71 wt%. The minimal weight loss below the decomposition temperature, along with the high T_{d10} and char yield, can be attributed to the material's high crosslinking density, which significantly enhances its thermal stability. Furthermore, powder X-ray diffraction (PXRD) analysis, presented in Fig. 2(c), confirmed the amorphous nature of

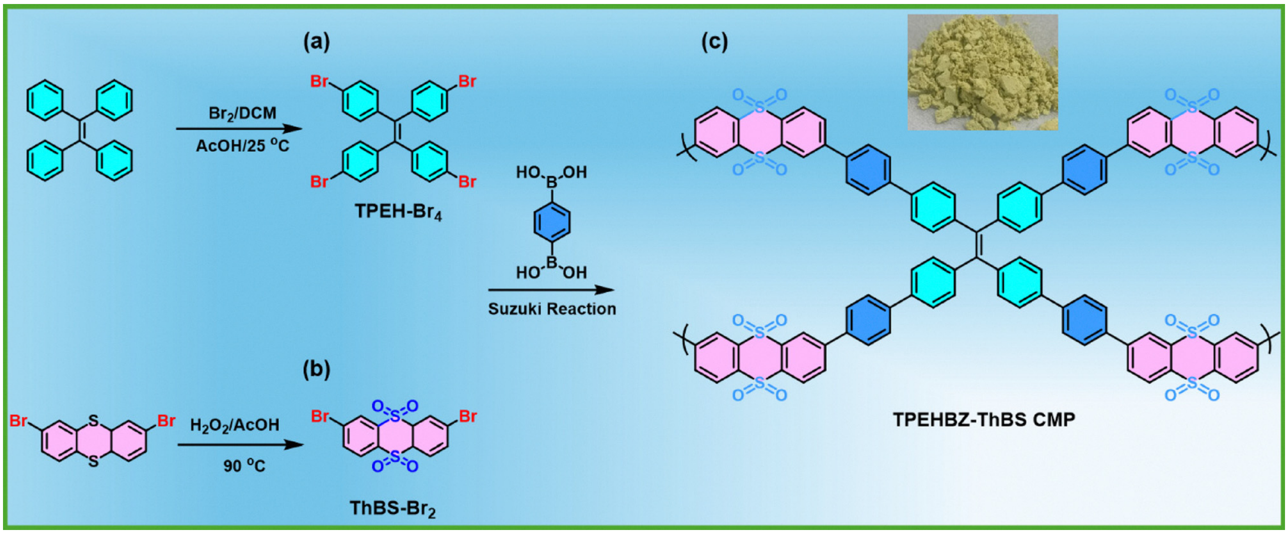

Fig. 1 The schematic of Suzuki coupling leading to the synthesis of (a) **TPEH-Br_4**, (b) **ThBS-Br_2**, and (c) **TPEHBZ-ThBS CMP**.

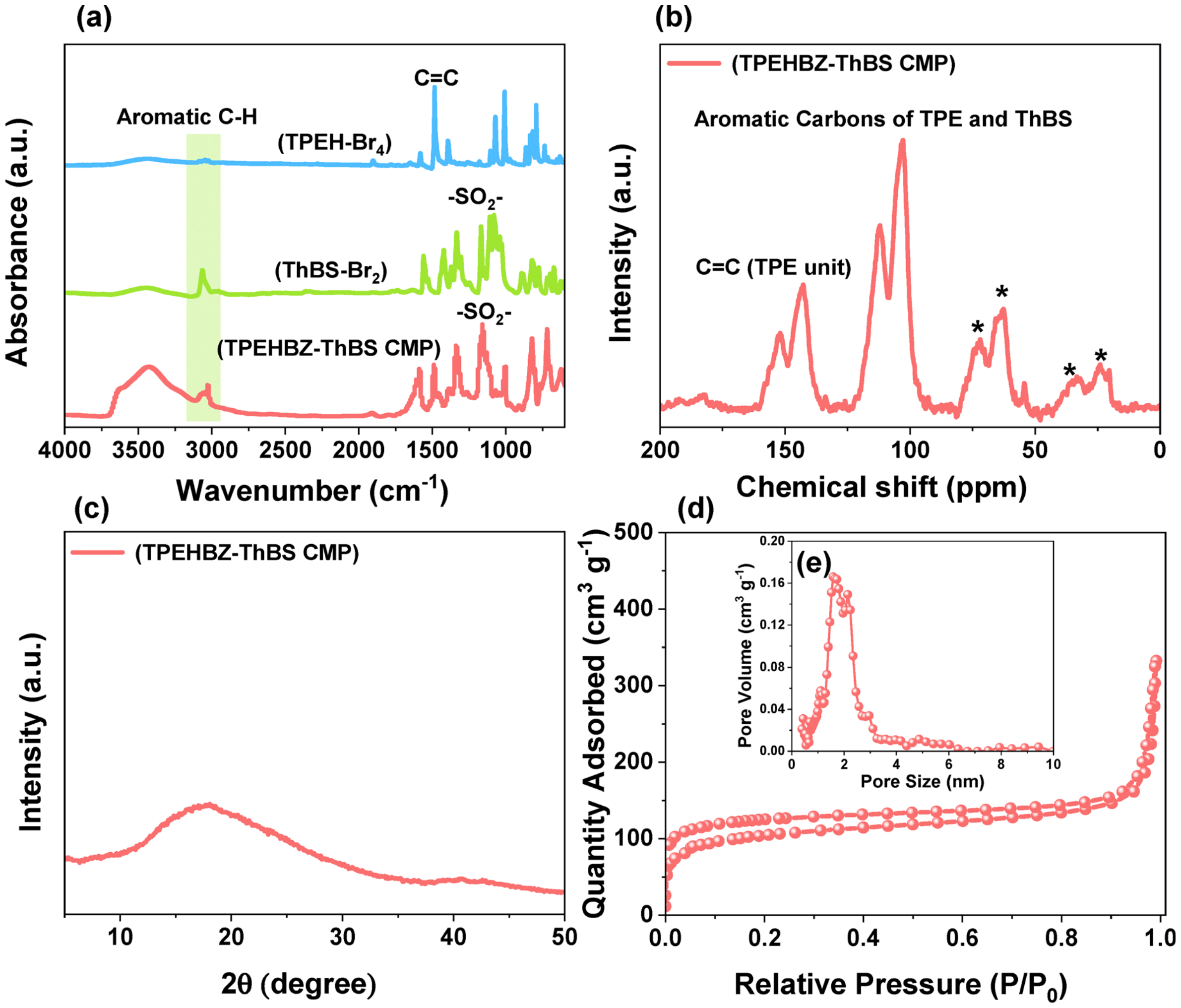

Fig. 2 (a) FT-IR spectra of **TPEH-Br$_4$**, **ThBS-Br$_2$**, and **TPEHBZ-ThBS CMP**. (b) Solid state ^{13}C NMR spectrum, (c) XRD pattern, and (d) N_2 adsorption/desorption isotherm; inset: (e) pore size distribution, recorded for the **TPEHBZ-ThBS CMP**.

the synthesized CMP. The porosity characteristics of the **TPEHBZ-ThBS CMP** were evaluated at 77 K by N_2 adsorption/desorption experiments. Fig. 2(d) shows that the adsorption isotherm combines Type I and Type IV characteristics (IUPAC), indicating micropores and mesopores. NLDFT analysis (Fig. 2(e)) reveals a primary pore size of 1.56 nm with additional peaks from 1.70 to 2.14 nm. The material has a BET surface area of 336 m^2 g^{-1} and a total pore volume (V_{total}) of 0.49 cm^3 g^{-1}. Such high surface area and pore features are expected to facilitate more capacitive charge storage, as they can lead to a larger contact area with the electrolyte. To investigate the elemental chemical states and interactions in the polymer, XPS analysis was conducted, as shown in Fig. 3(a). The survey spectrum of the **TPEHBZ-ThBS CMP** confirms the presence of sulfur, oxygen, and carbon. The high-resolution O 1s pattern displays a distinct peak at 531.7 eV, corresponding to the O═S bond [Fig. 3(b)]. In the C 1s spectrum, two distinct signals are detected at 283.6 and 284.3 eV, attributed to C═C and C–S bonds, respectively [Fig. 3(c)]. Additionally, the S 2p spectrum displays two signals at 167.5 and 168.6 eV, indicative of S–C and S═O bonds, respectively [Fig. 3(d)]. Fig. S7 (ESI†) depicts the SEM measurements of the **TPEHBZ-ThBS CMP**.

The SEM images, as shown in Fig. S7 (ESI†), reveal that the material consists of irregularly aggregated spheres. Additionally, SEM-EDS analysis [Fig. S8, ESI†] confirmed the presence of C (red color), O (blue color), and S (green color) elements within the **TPEHBZ-ThBS CMP** framework. These findings are consistent with the XPS results presented in Fig. 3, further validating the material's composition. TEM images [Fig. S9, ESI†] reveal that the micropores are homogenously distributed in the **TPEHBZ-ThBS CMP**. Thus, the above-mentioned results confirm the performed Suzuki coupling resulting in a conjugated microporous polymer containing tetraphenylethene and thianthrene-5,5′,10,10′-tetraoxide units. The fascinating functional groups are expected to result in better Li$^+$/Na$^+$ charge storage.

Electrochemical performances of the LIB and SIB using TPEHBZ-ThBS CMP

The lithium/sodium storage performances of the **TPEHBZ-ThBS CMP** anode were evaluated using CR-2032 coin-type half-cells (**TPEHBZ-ThBS CMP**|1 M LiPF$_6$|Li) and (**TPEHBZ-ThBS CMP**|1 M NaClO$_4$|Na). As a counter electrode, a Li/Na metal disc was used, while the working anode comprised a

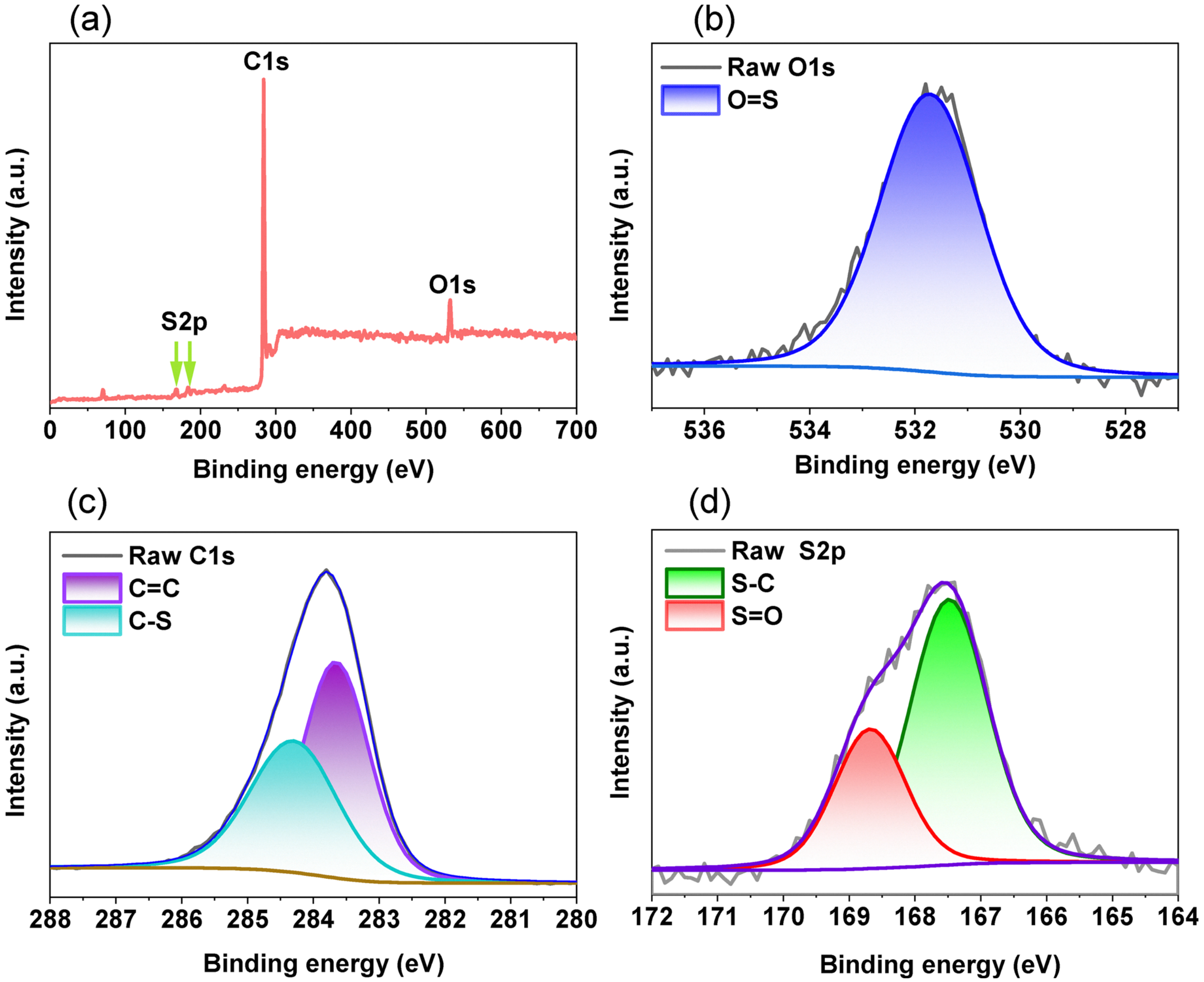

Fig. 3 (a) XPS survey spectrum of **TPEHBZ-ThBS CMP** and (b–d) deconvolution spectra of (b) O 1s, (c) C 1s, and (d) S 2p scan profiles recorded for the **TPEHBZ-ThBS CMP**.

TPEHBZ-ThBS CMP-coated electrode. The obtained CV and GCD profiles of the **TPEHBZ-ThBS CMP** anode are shown in Fig. 4. CV measurements were carried out at a scan rate of 0.1 mV s^{-1} within the potential range of 0.01–3.0 V for the LIB and 0.01–2.5 V for the SIB. The associated CV curves are shown in Fig. 4(a) and (b), for the LIB, during the first cathodic scan, strong current peaks appear within the 0.5–1.7 V potential range, indicating the formation of the solid electrolyte interface (SEI) layer.

This SEI layer typically consists of compounds such as Li_2O, Li_2CO_3 and LiF. A noticeable reduction in the current response of these cathodic peaks in the following CV cycles indicates stabilization of the SEI layer after its initial formation. Additional cathodic peaks at approximately 1.7 and 2.0 V (*versus* Li/Li^+) could be due to the redox activity of sulfonyl groups and possible Li^+ interactions with the conjugated polymer network. Furthermore, at the low-potential region (0.25–1.25 V), the CV profiles reveal a pair of asymmetric redox peaks and a favorable reduction process. The following electrochemical lithiation/de-lithiation of the **TPEHBZ-ThBS CMP** is believed to occur as outlined in eqn (1) and Fig. S10(a) (ESI†).

$$\textbf{TPEHBZ-ThBS CMP} + x\text{Li}^+ + xe^- \leftrightarrow \text{Li}_x(\textbf{TPEHBZ-ThBS CMP})^{x-} \quad (1)$$

Similarly, for the SIB during the initial cycle, prominent cathodic peaks appear in the range of 0.5–1.8 V, attributed to the formation of the SEI layer. The side reactions lead to the SEI layer, including the absorption of Na^+ ions and the generation of side products such as Na_2CO_3, and NaF, alongside the primary reaction mechanism described by eqn (2).[58] In the subsequent cycles, a noticeable reduction in the intensity of these cathodic peaks indicates the stabilization of the SEI layer, which is crucial for enhanced cycling stability. Additionally, smaller anodic and cathodic humps emerge at approximately 0.8 V and 1.0 V, respectively, throughout the CV cycles. These features are similar to the LIB and SIB corresponding to the reversible doping and de-doping of lithium-ions and sodium-

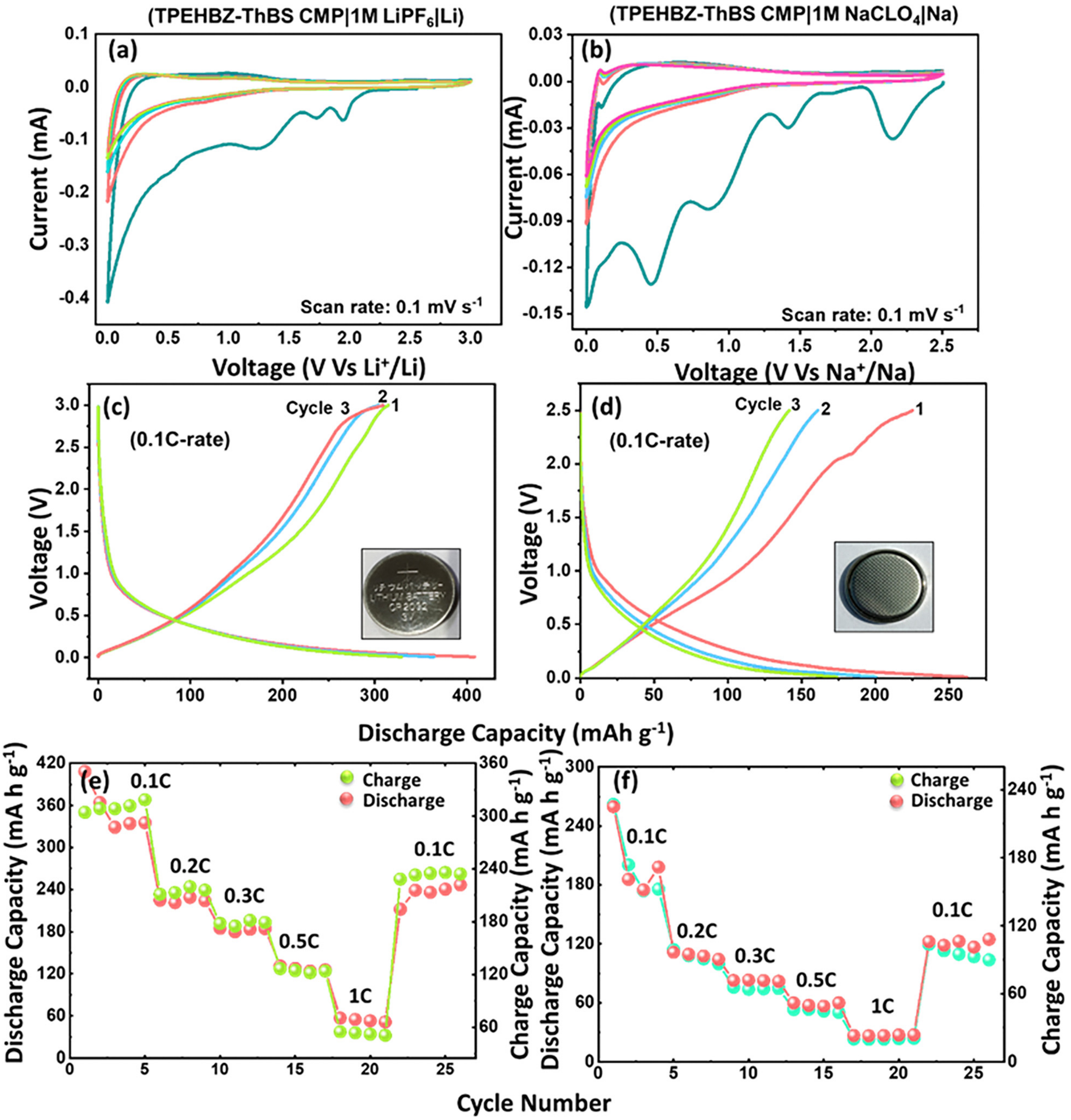

Fig. 4 (a) and (b) CV curves, (c) and (d) GCD plots, and (e) and (f) rate capability data recorded for the LIB (left) and SIB (right) comprising **TPEHBZ-ThBS CMP** as the anode and a lithium/sodium counter.

ions into and from the polymer chains. The sodium-ion storage mechanism underlying this behavior is described by eqn (2) and Fig. S10(b) (ESI†).

$$\textbf{TPEBZ-ThBS CMP} + x\mathrm{Na}^+ + xe^- \leftrightarrow \mathrm{Na}_x(\textbf{TPEHBZ-ThBS CMP})^{x-} \quad (2)$$

To quantify the Li^+/Na^+ charge storage, the galvanostatic charge–discharge profiles of the **TPEHBZ-ThBS CMP** anode were recorded at a 0.1C rate, and the obtained first three cycles are shown in Fig. 4(c) and (d). The detailed initial discharge profiles are presented in the ESI† [Fig. S11(a) and (b)]. Notably, the **TPEHBZ-ThBS CMP** anode exhibited an exceptionally high initial discharge capacity of 2958 and 1492 mAh g^{-1} for the LIB and SIB, respectively, which are typical for alternative anodes due to the interplay between Li^+/Na^+ insertion/de-insertion reactions and formation of the SEI layer. In subsequent cycles, the **TPEHBZ-ThBS CMP** anode displays a discharge capacity of 408 and 262 mAh g^{-1} for the LIB and SIB, respectively, at a 0.1C-rate, outperforming many previously reported organic anode materials. The initial coulombic efficiency (ICE) of the **TPEHBZ-ThBS** anode was determined to be 134 and 116% for the LIB and SIB from the first cycle charge–discharge profile in Fig. 4(c) and (d), respectively, with the subsequent cycles stabilizing close to 100%, which is typical for organic anode materials. The gradual activation of the electrode, where additional electrochemically active sites become available due to pore expansion and structural rearrangement during the initial cycles, leads to a slight increase in the CE, leading to excess apparent charge storage. The observed ICE is due to irreversible processes occurring predominantly during the first discharge cycle. These include the formation of the solid electrolyte interphase (SEI), electrolyte decomposition, and other side reactions typically seen in fresh electrode materials. The charging plateaus observed above 2.0 V in the GCD curves for both LIBs and SIBs originate from the adsorption/desorption-based charge storage mechanism rather than a distinct intercalation process. This is further supported by the cyclic voltammetry (CV) results, where no sharp redox peaks are observed, indicating the absence of well-defined phase transformations. The high specific capacity can be attributed to the high SA_{BET} and uniform microporous structure of the **TPEHBZ-ThBS CMP** framework, which provides numerous active sites for lithium/sodium storage. The coin cells were also tested at various C-rates to assess reversibility and rate capability, as illustrated in Fig. 4(e) and (f). The half-cells achieved discharge capacities of 408, 224, 184, 131, and 56 mAh g^{-1} for the LIB and 262, 114, 75, 53, and 23 mAh g^{-1} for the SIB at 0.1C, 0.2C, 0.3C, 0.5C, and 1C rates, respectively. Across all C-rates, the discharge profiles remained consistent, demonstrating strong reversibility and repeatability. The high specific capacity at low C-rates results from the full utilization of the active material. In contrast,

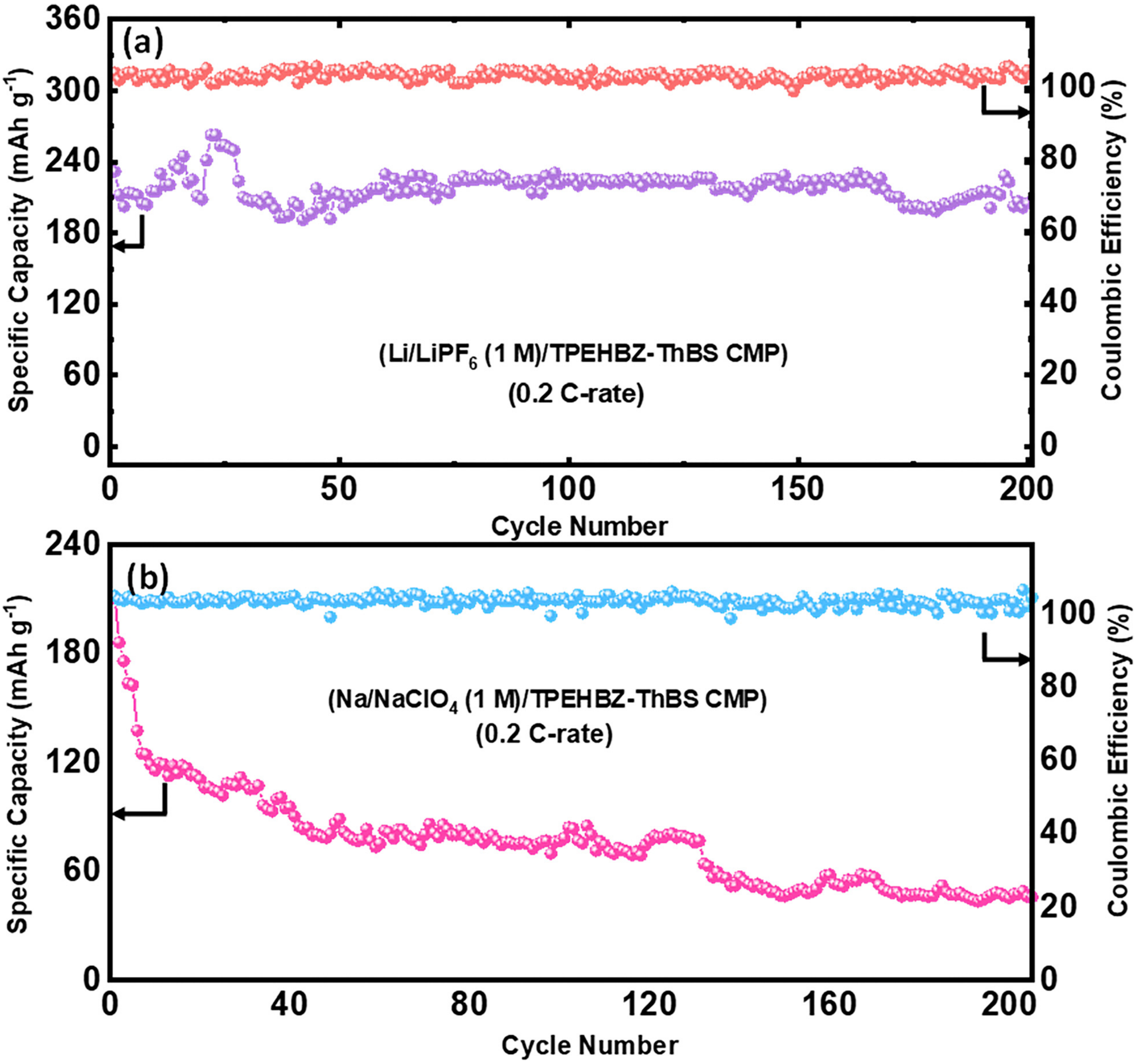

Fig. 5 Cycle-life data as well as coulombic efficiency at 0.2C-rate recorded for the (a) LIB and (b) SIB comprising the **TPEHBZ-ThBS CMP** as the anode and a lithium/sodium counter.

partial utilization of the active mass at higher C-rates leads to reduced capacity. Cycling stability over 200 charge–discharge cycles is shown in Fig. 5. At a 0.2C rate, the **TPEHBZ-ThBS CMP** anode stabilized at 225 mAh g^{-1} with 96% capacity retention for the LIB as shown in Fig. 5(a), whereas for the SIB as shown in Fig. 5(b), the capacity seemed to have faded due to electrode degradation. The inferior cyclability in the SIB could be attributed to the larger size of Na^+, which leads to fragile adsorption at the redox-active sites, making the storage process less stable and increasing the likelihood of quick desorption.[59] Another key factor is the solid electrolyte interphase (SEI) formation, which is often less stable in sodium-ion systems due to continuous electrolyte decomposition and side reactions, leading to irreversible capacity loss over cycling.[60] Furthermore, the π-conjugated backbone and redox units like tetraphenylethene and thianthrene tetraoxide of the CMP are less suited for efficient Na^+ hosting due to the lower charge density and slower diffusion kinetics of Na^+, contributing to reduced capacity retention and poor long-term cycling. While the capacity for SIBs is indeed lower, it is important to highlight that this work presents an early exploration of such CMPs as organic anode materials. The key merit of this material lies in its sustainability, structural tunability, and potential for mass production, which make it a promising candidate for LIBs and SIBs.

Additionally, the coulombic efficiency remained nearly 100% with slight variation throughout the cycle-life studies, indicative of side reactions and the dynamic nature of charge storage of lithium and sodium ions through surface adsorption and redox reactions rather than well-defined intercalation mechanisms for the **TPEHBZ-ThBS CMP** anode. Table 1 provides the literature on CMP-based anodes for LIBs and SIBs with their respective reported discharge capacities alongside the results of the present study. Notably, the discharge capacity of the **TPEHBZ-ThBS CMP** anode is either higher or comparable to the previously reported values.[48,50,61–64] As the cycling performance of the half-cell LIB showed a stable lithium charge storage capacity over 200 cycles, to test the practical viability, a full-cell was fabricated using the **TPEHBZ-ThBS CMP** anode, and commercial $LiNi_{0.8}Mn_{0.1}Co_{0.1}O_2$ (NMC811) cathode. The fabricated full cell (**TPEHBZ-ThBS CMP**|1 M $LiPF_6$|NMC811) was charged and discharged at a 0.1C-rate in a voltage window ranging from 1.5 to 4.5 V. This voltage window was chosen from the half-cell studies as well as the literature. The full cell exhibits an initial charge capacity of 128 mAh g^{-1} and discharge capacity of 122 mAh g^{-1} at 0.1C-rate. The above-mentioned three galvanostatic charge–discharge cycles of the full cell are depicted in Fig. S12 (ESI†). Almost all three invariant cycles, charging curves as well as discharging curves confirm that the full cell exhibits stable and reversible Li^+ charge storage with discharge capacity as high as 122 mAh g^{-1}. The full cell was used to power a green LED bulb, and it could glow for over 3 h on a single charge. Thus, this study implies that the **TPEHBZ-ThBS CMP** anode can be used as an alternate anode for LIBs. The capacity obtained in the present work is significantly high. Enhanced performance is ascribed to the SO_2 units in the **TPEHBZ-ThBS CMP** framework, which likely contribute to improved discharge capacity and stability by offering additional active sites and enhancing the structural integrity during cycling.

Table 1 Literature on CMP-based anodes for LIBs and SIBs with their respective reported discharge capacities alongside the results of the present study. Notably, the discharge capacity of the **TPEHBZ-ThBS CMP** anode is either higher or comparable to the previously reported values[48,50,61–64]

CMP electrode material	Battery type	Electrochemical potential window (V)	Discharge capacity (mAh g^{-1})	Ref.
PDCzBT	Sodium-ion	0.01–3.0	150 at 50 mA g^{-1}	48
DBD	Lithium-ion	0.01–3.0	561 at 50 mA g^{-1}	50
PBAPD-AQ	Lithium-ion	0.01–3.0	220 at 500 mA g^{-1}	61
NPCs	Sodium-ion	0.01–3.0	237.7 at 50 mA g^{-1}	62
CONs	Sodium-ion	0.01–2.5	250 at 100 mA g^{-1}	63
PDCzBT	Lithium-ion	0.01–3.0	400 at 100 mA g^{-1}	48
Co-PCMPs	Lithium-ion	0.01–3.0	488 at 50 mA g^{-1}	64
TPEHBZ-ThBS	**Lithium-ion**	**0.01–3.0**	**408 at 0.1C**	**This work**
TPEHBZ-ThBS	**Sodium-ion**	**0.01–2.5**	**262 at 0.1C**	**This work**

Capacitive and diffusive contribution analysis for LIBs and SIBs using TPEHBZ-ThBS CMP

The nature of the CV profiles reveals not only faradaic storage for the Li^+/Na^+ capacity, but there seems to be a capacitive storage as well. To confirm and quantify the same, comprehensive CV analyses were performed on the LIB and the SIB half-cells across a range of low scan rates (0.05–1 mV s^{-1}) to deconvolute diffusive and capacitive charge storage. This analysis utilized Dunn's method and Power Law, whose results are illustrated in Fig. 6. For LIBs and SIBs, the CV profiles in Fig. 6(a) and Fig. S13(a) (ESI†) display distinct redox peaks consistently observed at all tested low scan rates, indicating stable and reproducible electrochemical behavior. Fig. 6(b) and Fig. S13(b) (ESI†) present the Randles–Sevcik plots, which were used to analyze the relationship between scan rate and peak current based on the CV data. A linear increase in peak current with the scan rate was observed, indicating that the occurrence of definitely reversible redox reactions is an essential attribute of a functional battery electrode. The power law was utilized for quantitatively distinguishing between capacitive and diffusive charge storage contributions. This analysis provides deeper insights into the relative significance of surface-controlled processes and bulk ion diffusion, further elucidating the charge storage mechanisms within the **TPEHBZ-ThBS CMP** material. The power law can be stated as shown below:[65]

$$i = a\nu^{b}$$

$$\log(i) = \log a + b\log(\nu)$$

where a and b are constants and i and ν represent the peak current (in A) and scan rate (in mV s^{-1}). The slope of the $\log(i)$ *vs.* $\log(\nu)$ linear plot can be used to get the constant b, and the intercept can be used to determine the constant a. If $b = 0.5$, the electrode is considered to be diffusive; if $b = 1.0$, it is said to be

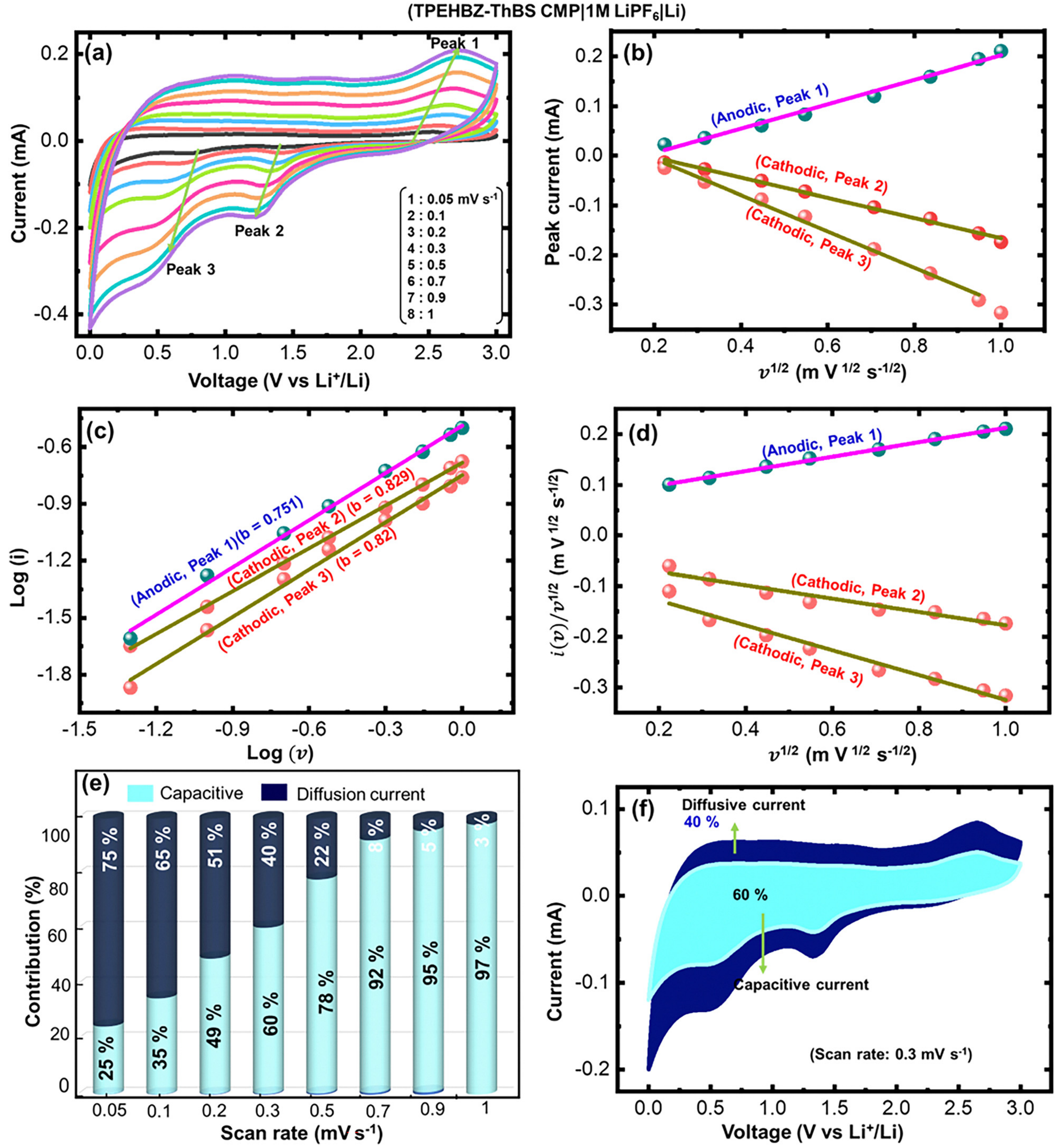

Fig. 6 (a) CV profiles of **TPEHBZ-ThBS CMP** for LIBs, (b) Randles plot, (c) power law plot, and (d) Dunn's plot of the **TPEHBZ-ThBS CMP**. (e) Proportion of capacitive behavior in **TPEHBZ-ThBS CMP** under varying scan rates. (f) Contribution from capacitance in the **TPEHBZ-ThBS CMP** anode at 0.3 mV s^{-1}, for LIBs.

capacitive. The calculated slope values for the anodic and cathodic peaks from the power-law linear plots are 0.751 and 0.829 for the LIB, and 0.593 and 0.618 for the SIB, respectively, as shown in Fig. 6(c) and Fig. S13(c) (ESI†). These values indicate that charge storage in both the LIB and SIB involves a combination of diffusion and capacitive-controlled mechanisms, where the diffusive mode serves as the foremost contributor. To further quantify capacitive and diffusive contributions in the storage of Li^+/Na^+ charge on the **TPEHBZ-ThBS CMP** electrode, Dunn's approach was employed. This method asserts that the total current *i*, observed at any potential in the cyclic voltammetry (CV) profile, arises from the composition of two processes, namely capacitive and diffusive, which is described by the following relationship:[66]

$$i(\nu) = i_{\text{cap}} + i_{\text{diff}}$$

$$i(\nu) = k_1\nu + k_2\nu^{1/2} \quad \text{or} \quad \frac{i(\nu)}{\nu^{1/2}} = k_1\nu^{1/2} + k_2$$

where k_1 and k_2 are constants, $i(\nu)$ represents the total current, i_{cap} represents the capacitive current contribution attained as a result of double-layer storage, and i_{diff} represents the diffusive current contribution as a result of the faradaic reactions. Dunn's plots are linear graphs of $(i/\nu^{1/2})$ *vs.* $(\nu^{1/2})$, which are shown in Fig. 6(d) and Fig. S13(d) (ESI†). It is utilized to quantitatively analyze the contributions from both diffusive and capacitive currents by varying the scan rates (noted only at low scan rates) based on the slope values. The corresponding bar diagrams in Fig. 6(e) and Fig. S13(e) (ESI†) illustrate these contributions. At lower 0.05 mV s^{-1}, the diffusion process dominates the charge storage, contributing up to 75% for the LIB and 89% for the SIB. Conversely, at higher scan rates (1 mV s^{-1}), capacitive contributions become more significant, reaching 97% for the LIB and 49% for the SIB, while diffusive contributions decreased to 3% and 51%, respectively. The rapid transition from diffusive to capacitive contributions observed at relatively low scan rates primarily relies on the charge storage mechanism in CMPs predominantly being adsorption/desorption rather than a well-defined, highly reversible intercalation/deintercalation or conversion process. The difference in capacitive contribution between LIBs (97%) and SIBs (49%) at a high scan rate (1.0 mV s^{-1}) can be partially attributed to the steric hindrance and limited diffusion pathways within the porous structure of the CMP for Na^+ transport due to its larger ionic size and lower mobility, leading to a lower capacitive contribution. The CV profiles for the LIB and SIB cells at 0.3 mV s^{-1}, shown in Fig. 6(f) and Fig. S13(f) (ESI†), reveal a diffusive contribution of 40% and 73% and a capacitive contribution of 60% and 27%, respectively. The Li^+/Na^+ diffusion kinetics at the electrode interfaces were evaluated using EIS on both the coin cells, and the corresponding Nyquist plots are presented in Fig. S14 (ESI†). The high-frequency region of the plots features a distinct semicircle, and the diameter represents resistance at the interface of the electrode/electrolyte. In the low-frequency region, a spike that is angled around 45° to the *x*-axis signifies the Warburg element, associated with Li^+/Na^+ diffusion and charge transfer processes as shown in Fig. S14(a) and (b) (ESI†).[67] The Nyquist plots were interpreted based on the equivalent circuit shown in the inset of Fig. S14 (ESI†). The charge transfer resistance (R_{ct}) values derived from the fitting reveal variations due to electrode/electrolyte degradation, a common occurrence in battery systems during repeated charge–discharge cycling. Notably, the R_{ct} for the sodium-ion cell was found to be slightly higher than that for the lithium-ion cell. This difference can be attributed to factors such as more pronounced concentration polarization and their inherent ionic conductivities. These results underscore the role of ion transport properties in governing the interfacial charge transfer kinetics in LIBs and SIBs. At low frequencies, Li^+ and Na^+ ion transport through the electrode materials becomes apparent. Eqn (S4) (ESI†) was used to calculate the ion diffusion coefficient from the low-frequency portion of the EIS spectra.[68] The following equation, in which ω stands for the angular frequency in the low-frequency area, is associated with the Warburg factor (σ).[69]

$$Z' \propto \sigma\omega^{-1/2}$$

The slope of this linear equation of Z' and $\omega^{-1/2}$ corresponds to σ, which is connected to the ion diffusion in the electrode material. The computed σ for the LIB and SIB is 418 913 and 38 387, respectively, as illustrated in Fig. S15 (ESI†). As a result, the diffusion coefficient (D_{Li^+}) value for the LIB is calculated to be 4.87×10^{-15} cm^2 s^{-1} and that for the SIB is calculated to be 4.09×10^{-17} cm^2 s^{-1}, respectively. Thus, the superior capacity of the **TPEHBZ-ThBS CMP** electrode is attributed to its ability to accommodate Li^+ ions more efficiently than Na^+ ions, enabling smoother migration pathways within the electrode structure.

Post-cycling analysis of the cycled TPEHBZ-ThBS CMP electrode

The CR-2032 cells of the LIB and SIB were tested after cycle life studies to gain insight into the structural stability and charge storage abilities of the cycled **TPEHBZ-ThBS CMP** electrodes. Consequently, FT-IR and SEM analyses were performed. Fig. S16 (ESI†) depicts the FT-IR spectra obtained post-cycling for the **TPEHBZ-ThBS CMP** electrodes. In Fig. S16(a) (ESI†) the peak at 1139 cm^{-1} corresponds to asymmetric S–O stretching in Li^+-coordinated sulfonyl groups, while the peak at 1044 cm^{-1} is due to symmetric S–O stretching, both shifted from 1160 cm^{-1} due to Li^+ coordination, indicating increased ionic character. The sharp peak at 1387 cm^{-1} arises from $-CH_2$ in the PVDF binder. Peaks at 1634, 1290, and 883 cm^{-1} are attributed to polycarbonate species formed from electrolyte solvents. Similarly, in the Na^+ system [Fig. S16(b), ESI†], the bands at 1085 cm^{-1} correspond to symmetric S–O stretching in Na^+-coordinated sulfonyl groups, shifted from 1160 cm^{-1}, indicating Na^+ coordination. The absorption band at 1407 cm^{-1} is from PVDF, and the peaks at 1591 and 877 cm^{-1} are due to polycarbonate species. Thus, it was noted that the sulfonyl groups present in the CMP enhanced the charge-storage mechanism due to effective coordination with Li^+ and Na^+ ions, thereby contributing to the cell capacity. Furthermore, based on the SEM morphological analysis after cyclic stability tests for LIBs and SIBs using **TPEHBZ-ThBS CMP**, as shown in Fig. S17 (ESI†), we observed that the **TPEHBZ-ThBS CMP** anode in the LIBs retained their morphology, indicating good structural stability and minimal degradation. This suggests that the CMP framework remains robust during repeated Li^+ insertion and extraction, and the capacity loss after high-rate cycling is likely due to kinetic limitations rather than structural degradation. In contrast, the **TPEHBZ-ThBS CMP** anode morphology in SIBs changed noticeably after cycling, suggesting possible structural degradation. This can be attributed to the larger ionic radius of Na^+ (1.02 Å) compared to Li^+ (0.76 Å), which can cause greater mechanical strain and disruption of the polymer framework during repeated adsorption/desorption. Additionally, weaker interactions between Na^+ and the CMP backbone may lead to poor anchoring and faster desorption, destabilizing the structure over prolonged cycling. Thus, the difference in post-cycling morphology supports the conclusion that the material exhibits good electrochemical and structural stability in LIBs, while the degradation observed in SIBs is due to the inherent size and interaction limitations of Na^+ ions within the polymeric matrix.

Theoretical studies on the TPEHBZ-ThBS CMP

We conducted DFT calculations on the individual building units as well as on the polymers to analyze their geometrical structures and electronic properties. The HOMO and LUMO energies of these molecules were calculated at the B3LYP-D3(BJ)/6-31G(d) level of theory.[70,71] Fig. S18 (ESI†) presents the HOMO–LUMO isosurface maps for TPEBHZ and the ThBS unit, revealing critical insights into their electronic and orbital distributions. Both building blocks exhibit high conjugation, with the HOMO and LUMO delocalized across their respective conjugated systems. Fig. 7 illustrates the orbital distributions for the three polymers. For **TPEHBZ-ThBS CMP**, the HOMO is predominantly localized on the biphenyl moiety, while the LUMO is concentrated on the ThBS arm. In **TPEHBZ-ThBS/Li$^+$**, the HOMO is localized around the ThBS/Li$^+$ groups, whereas the LUMO is distributed across the three benzene rings. Similarly, for **TPEHBZ-ThBS**/Na$^+$, both the HOMO and LUMO are localized on the ThBS/Na$^+$ groups. The calculated HOMO–LUMO energy gaps are 3.53 eV for TPEHBZ and 5.54 eV for the ThBS unit. Upon polymerization, the energy gaps for **TPEHBZ-ThBS CMP**, **TPEHBZ-ThBS CMP/Li$^+$**, and **TPEHBZ-ThBS CMP/Na$^+$** are reduced to 4.00 eV, 2.54 eV, and 0.74 eV, respectively. This reduction in the HOMO–LUMO gap, attributed to extended conjugation in the polymeric structures, enhances electronic conductivity and charge transfer efficiency, which are critical for high-performance electrode materials. Additionally, the Li and Na derivatives exhibit lower energy gaps compared to the unmodified CMP, further emphasizing their altered electronic properties and highlighting their significant role in facilitating ion interactions and ability to effectively store and release charge, contributing to enhanced specific capacities of the LIB and SIB. Fig. S19 (ESI†) shows molecular electrostatic potential (MESP) analysis of the building units, providing a numerical visualization of electrophilic and nucleophilic sites within the molecules. The MESP maps identify the most reactive regions, with red areas indicating high electron density (negative electrostatic potential, nucleophilic) and blue areas representing low electron density (positive electrostatic potential, electrophilic). In TPEHBZ, the highest electron densities (dense red regions) are concentrated around the π-electrons of the benzene rings, corresponding to the most nucleophilic sites. Conversely, the terminal hydrogens of the phenyl groups exhibit the highest positive potential, marking them as electrophilic. For the ThBS unit, the electrostatic potential values are more pronounced, reflecting the electron-withdrawing nature of the sulfonyl groups. The negative potential ranges from −30 to −46 kcal mol^{-1}, while the terminal hydrogens show a positive potential of approximately 26 kcal mol^{-1}. The MESP maps of the **TPEHBZ-ThBS CMP**, **TPEHBZ-ThBS CMP/Li$^+$**, and **TPEHBZ-ThBS CMP/Na$^+$** were acquired. In all cases, the highest negative potentials are localized around the SO_2, ThBS/Li$^+$, and ThBS/Na$^+$ groups, with values of −48, −53, and −40 kcal mol^{-1}, respectively. In the case of the **TPEHBZ-ThBS CMP/Li$^+$** and **TPEHBZ-ThBS CMP/Na$^+$**, the highest positive electrostatic potentials are concentrated around the Li and Na atoms, measuring 170 and 110 kcal mol^{-1}, respectively, indicating strong electrostatic interactions with anions, which facilitate ionic conduction in the LIB and SIB. Notably, the higher positive potential of Li^+ (170 kcal mol^{-1}) compared to Na^+ (110 kcal mol^{-1}) aligns with the higher specific capacity of 408 mAh g^{-1} for the LIB, as Li^+ forms stronger ionic bonds and enables more efficient electron transport. These findings highlight the significant influence of the sulfonyl groups and metal atoms on the electrostatic potential distribution and reactivity of the CMPs. Table S1 (ESI†) shows the calculated global

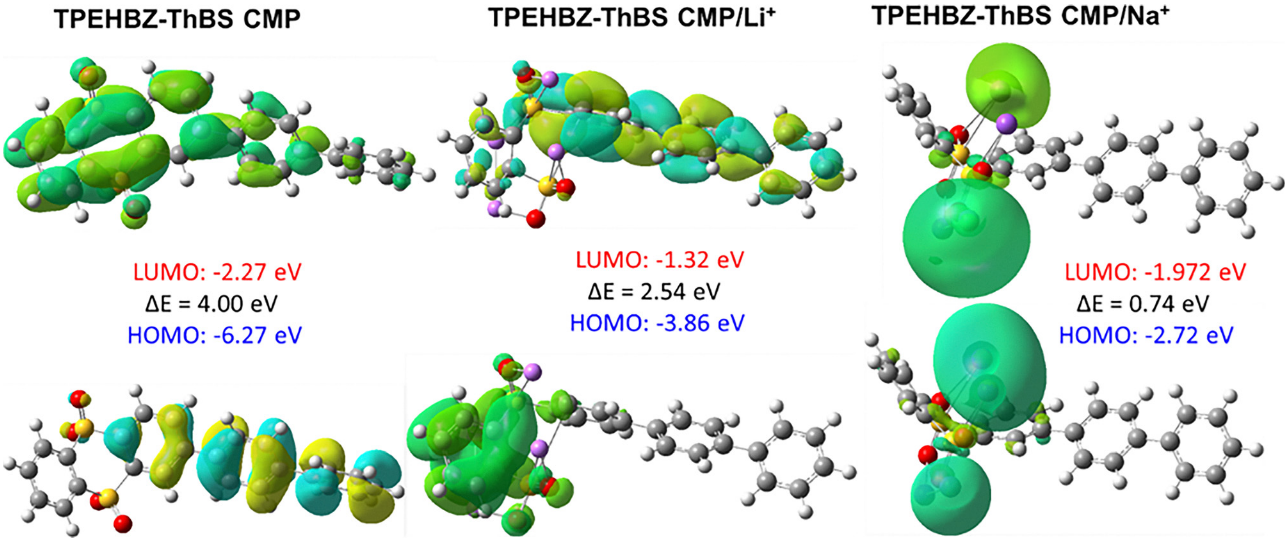

Fig. 7 The HOMO and LUMO isosurface maps of a representative model of **TPEHBZ-ThBS CMP**, **TPEHBZ-ThBS CMP/Li$^+$**, and **TPEHBZ-ThBS CMP/Na$^+$**, along with their energies calculated at the B3LYP-D3(BJ)/6-31G(d) level.

reactivity descriptors. Calculations were performed using DFT at the same level using the equations.[72] The energy of the HOMO (E_{HOMO}) and LUMO (E_{LUMO}) is an indication of the molecule's tendency for donating and accepting electrons, respectively. The HOMO–LUMO gap, which is the energy difference between the two orbitals, is an indication of the molecule's reactivity: the smaller the gap, the higher the reactivity. As shown in Table S1 (ESI†), **TPEHBZ-ThBS CMP/Na$^+$** has the highest E_{HOMO} (lowest ionization potential, IP), which indicates that it is the best electron donor. The lowest E_{LUMO} (highest electron affinity, EA) among the polymers is **TPEHBZ-ThBS CMP**. The **TPEHBZ-ThBS CMP** with Na has the smallest gap and thus is the most reactive. It also has the lowest electronegativity, χ, the highest electrophilicity index, ω, and the highest capacity for charge transfer (highest ΔN_{max}). Thus, these findings validate the reactivity, charge transfer rates, and overall performance of the **TPEHBZ-ThBS CMP** in the LIB and SIB.

Conclusions

In conclusion, we successfully synthesized a **TPEHBZ-ThBS CMP** *via* the Suzuki coupling reaction and demonstrated its potential as an organic anode material for LIBs and SIBs through detailed electrochemical evaluation. The presence of the sulfonyl groups in the **TPEHBZ-ThBS CMP** structure enabled strong binding with Li^+ and Na^+ ions, facilitating smooth charge transport. The CR-2032 coin cells that contained **TPEHBZ-ThBS CMP** as an anode exhibited impressive electrochemical performance, achieving a high reversible capacity of 408 and 262 mAh g^{-1} for LIBs and SIBs at a 0.1C-rate. After 100 cycles, the LIB retained 96% of its capacity. Additionally, the lithium-ion full cell fabricated using NMC811 as a cathode and **TPEHBZ-ThBS CMP** as an anode exhibited a discharge capacity of 122 mAh g^{-1} at 0.1C-rate. Furthermore, evaluations employing the power law and Dunn's approach revealed a synergistic contribution of both diffusive and capacitive charge storage mechanisms, further enhancing cell performance. The MESP maps and the DFT calculations revealed that the presence of sulfonyl groups facilitated high positive electrostatic potentials, high electrophilicity, and capacity for charge transfer, resulting in enhanced overall performance. These findings highlight **TPEHBZ-ThBS CMP** as a prospective anode material for SIBs and LIBs, offering advantages such as excellent structural properties, facile synthesis, favorable surface area, and optimized morphology. Thus, the **TPEHBZ-ThBS CMP** can be a compelling candidate for organic electrode materials in advanced energy storage systems.

Author contributions

Bhargabi Halder: investigation, methodology, conceptualization, writing – original draft. Mohamed Gamal Mohamed: investigation: methodology, conceptualization, supervision, writing – original draft. Kalidoss Kannadasan: investigation. Ahmed A. K. Mohammed: investigation. Poonam Nagendra Singh: investigation. Tapomay Mondal: investigation. Yunsheng Ye: investigation. Perumal Elumalai: supervision. Shiao-Wei Kuo: supervision.

Conflicts of interest

There are no conflicts to declare.

Data availability

Data will be made available on request.

Acknowledgements

This study was supported financially by the National Science and Technology Council, Taiwan, under contracts NSTC 113-2223-E-110-001- and 113-2221-E-110-012-MY3. The authors thank the Science and Engineering Research Board (SERB), Government of India, under the research grant (CRG/2021/005678) and Central Power Research Institute, Bangalore (CPRI) under the research grant (CPRI/R&D/TC/GDEC/2023). The authors thank the staff at National Sun Yat-sen University for their assistance with the TEM (ID: EM022600) experiments. The authors thank the staff at National Sun Yat-sen University for their assistance with the TEM (ID: EM022600) experiments.

Notes and references

1 M. M. Samy, M. G. Mohamed, S. U. Sharma, S. V. Chaganti, J. T. Lee and S. W. Kuo, An Ultrastable Tetrabenzonaphthalene-Linked conjugated microporous polymer functioning as a high-performance electrode for supercapacitors, *J. Taiwan Inst. Chem. Eng.*, 2024, **158**, 104750, DOI: 10.1016/j.jtice.2023.104750.

2 J. Libich, J. Máca, J. Vondrák and J. M. Sedlaříková, Supercapacitors: Properties and applications, *J. Energy Storage*, 2018, **17**, 224–227, DOI: 10.1016/J.est.2018.03.012.

3 S. H. Wang, L. Li, H. Wang, X. W. Wang and T. H. Wang, Continuous and Scalable Manufacture of Coal-Derived Hierarchical Porous Carbon Dominated with Mesopores for High Rate-Performance Supercapacitors, *ACS Appl. Energy Mater.*, 2024, **7**, 4268–4278, DOI: 10.1021/acsaem.4c00711.

4 M. G. Mohamed, A. Basit, C. Y. Shih, S. U. Sharma, T. Mondal and S. W. Kuo, Pyrene-Linked Covalent Organic Polymer/Single-Walled Carbon Nanotubes Hybrids as High-Performance Electrodes for Supercapacitive Energy Storage, *ACS Appl. Energy Mater.*, 2025, **8**, 3764–3778, DOI: 10.1021/acsaem.5c00052.

5 M. Ejaz, M. G. Mohamed, Y. T. Chen, K. Zhang and S. W. Kuo, Porous carbon materials augmented with heteroatoms derived from hyperbranched biobased benzoxazine resins for enhanced CO_2 adsorption and exceptional supercapacitor performance, *J. Energy Storage*, 2024, **78**, 110166, DOI: 10.1016/j.est.2023.110166.

6 A. O. Mousa, S. U. Sharma, S. V. Chaganti, T. H. Mansoure, P. N. Singh, M. Ejaz, C. H. Chuang, J. T. Lee, S. W. Kuo and

M. G. Mohamed, Designing strategically functionalized conjugated microporous polymers with pyrene and perylenetetracarboxylic dianhydride moieties with single-walled carbon nanotubes to enhance supercapacitive energy storage efficiency, *J. Power Sources*, 2024, **608**, 234624, DOI: **10.1016/j.jpowsour.2024.234624**.

7 M. G. Mohamed, C. C. Chen and S. W. Kuo, Nitrogen and sulfur co-doped microporous carbon through benzo[c]-1,2,5-thiadiazole-functionalized benzoxazine-linkage porous organic polymer in CO_2 capture and energy storage, *React. Funct. Polym.*, 2025, **214**, 106286, DOI: **10.1016/j.reactfunctpolym.2025.106286**.

8 S. V. Chaganti, S. U. Sharma, M. Ibrahim, A. Basit, P. N. Singh, S. W. Kuo and M. G. Mohamed, Redox-active a pyrene-4,5,9,10-tetraone and thienyltriazine-based conjugated microporous polymers for boosting faradaic supercapacitor energy storage, *J. Power Sources*, 2025, **627**, 235848, DOI: **10.1016/j.jpowsour.2024.235848**.

9 Q. Yuan, C. Li, X. Guo, J. Zhao, Y. Zhang, B. Wang, Y. Dong and L. Liu, Electrochemical Performance and Storage Mechanism Study of Conjugate Donor–Acceptor Organic Polymers as Anode Materials of Lithium-Ion Battery, *Energy Rep.*, 2020, **6**, 2094–2105, DOI: **10.1016/j.egyr.2020.08.001**.

10 S. Punyasloka, K. Higashimine and N. Matsumi, Donor–Acceptor-Based Conjugated Polymeric Active Material with Enhanced Pseudocapacitive Contribution for Ultrafast Charging of Lithium-Ion Batteries, *ACS Appl. Energy Mater.*, 2024, **7**, 5379–5389, DOI: **10.1021/acsaem.4c00404**.

11 M. M. Samy, M. G. Mohamed and S. W. Kuo, Pyrene-functionalized tetraphenylethylene polybenzoxazine for dispersing single-walled carbon nanotubes and energy storage, *Compos. Sci. Technol.*, 2020, **199**, 108360, DOI: **10.1016/j.compscitech.2020.108360**.

12 J. Liu, J. Wang, C. Xu, H. Jiang, C. Li, L. Zhang, J. Lin and Z. X. Shen, Advanced Energy Storage Devices: Basic Principles, Analytical Methods, and Rational Materials Design, *Adv. Sci.*, 2018, **5**, 1700322, DOI: **10.1002/advs.201700322**.

13 B. Halder, M. G. Mohamed, S. W. Kuo and P. Elumalai, Review on composite polymer electrolyte using PVDF-HFP for solid-state lithium-ion battery, *Mater. Today Chem.*, 2024, **36**, 101926, DOI: **10.1016/j.mtchem.2024.101926**.

14 X. Guan, Y. Zhao, H. Pei, M. Zhao, Y. Wang, X. Zhou, M. G. Mohamed, S. W. Kuo and Y. Ye, Metalloporphyrin conjugated porous polymer in-situ grown on a Celgard separator as multifunctional polysulfide barrier and catalyst for high-performance Li-S batteries, *Chem. Eng. J.*, 2023, **473**, 144733, DOI: **10.1016/j.cej.2023.144733**.

15 Y. Ye, M. G. Mohamed, W. C. Chen and S. W. Kuo, Integrating the multiple functionalities in metalloporphyrin porous organic polymers enabling strong polysulfide anchoring and rapid electrochemical kinetics in Li–S batteries, *J. Mater. Chem. A*, 2023, **11**, 9112–9124, DOI: **10.1039/D2TA09232H**.

16 T. L. Kulova, V. N. Fateev, E. A. Seregina and A. S. Grigoriev, A Brief Review of Post-Lithium-Ion Batteries, *Int. J. Electrochem. Sci.*, 2020, **15**, 7242–7259, DOI: **10.20964/2020.08.22**.

17 J. W. Choi and D. Aurbach, Promise and reality of post-lithium-ion batteries with high energy densities, *Nat. Rev. Mater.*, 2016, **1**, 1–16, DOI: **10.1038/natrevmats.2016.13**.

18 J. Y. Hwang, S. T. Myung and Y. K. Sun, Sodium-ion batteries: present and future, *Chem. Soc. Rev.*, 2017, **46**, 3529–3614, DOI: **10.1039/C6CS00776G**.

19 H. Kim, J. Hong, G. Yoon, H. Kim, K. Y. Park, M. S. Park, W. S. Yoon and K. Kang, Sodium intercalation chemistry in graphite, *Energy Environ. Sci.*, 2015, **8**, 2963–2969, DOI: **10.1039/C5EE02051D**.

20 Z. L. Xu, G. Yoon, K. Y. Park, H. Park, O. Tamwattana, S. J. Kim, W. M. Seong and K. Kang, Tailoring sodium intercalation in graphite for high energy and power sodium ion batteries, *Nat. Commun.*, 2019, **10**, 2598, DOI: **10.1038/s41467-019-10551-z**.

21 X. Li, X. Wang and J. Sun, Recent progress in the carbon-based frameworks for high specific capacity anodes/cathode in lithium/sodium ion batteries, *New Carbon Mater.*, 2021, **36**, 106–116, DOI: **10.1016/S1872-5805(21)60008-2**.

22 M. G. Mohamed, T. H. Mansoure, M. M. Samy, Y. Takashi, A. A. K. Mohammed, T. Ahamad, S. M. Alshehri, J. Kim, B. M. Matsagar, K. C. W. Wu and S. W. Kuo, Ultrastable Conjugated Microporous Polymers Containing Benzobisthiadiazole and Pyrene Building Blocks for Energy Storage Applications, *Molecules*, 2022, **27**, 2025, DOI: **10.3390/molecules27062025**.

23 M. G. Mohamed, S. U. Sharma, N. Y. Liu, T. H. Mansoure, M. M. Samy, S. V. Chaganti, Y. L. Chang, J. T. Lee and S. W. Kuo, Ultrastable Covalent Triazine Organic Framework Based on Anthracene Moiety as Platform for High-Performance Carbon Dioxide Adsorption and Supercapacitors, *Int. J. Mol. Sci.*, 2022, **23**, 3174, DOI: **10.3390/ijms23063174**.

24 A. O. Mousa, M. G. Mohamed, C. H. Chuang and S. W. Kuo, Carbonized Aminal-Linked Porous Organic Polymers Containing Pyrene and Triazine Units for Gas Uptake and Energy Storage, *Polymers*, 2023, **15**, 1891, DOI: **10.3390/polym15081891**.

25 M. C. Lin, S. W. Kuo and M. G. Mohamed, High-Performance Anthracene-Linked Covalent Triazine Framework with Dual Functions for CO_2 Capture and Supercapacitor Applications, *Mater. Adv.*, 2024, **5**, 6222–6233, DOI: **10.1039/D4MA00565A**.

26 K. Amin, N. Ashraf, L. Mao, C. F. J. Faul and Z. Wei, Conjugated microporous polymers for energy storage: Recent progress and challenges, *Nano Energy*, 2021, **85**, 105958, DOI: **10.1016/j.nanoen.2021.105958**.

27 M. G. Mohamed, M. M. Samy, T. H. Mansoure, S. U. Sharma, M. S. Tsai, J. H. Chen, J. T. Lee and S. W. Kuo, Dispersions of 1,3,4-oxadiazole-linked conjugated microporous polymers with carbon nanotubes as a high-performance electrode for supercapacitors, *ACS Appl. Energy Mater.*, 2022, **5**, 3677–3688, DOI: **10.1021/acsaem.2c00100**.

28 M. G. Mohamed, C. C. Chen, M. Ibrahim, A. O. Mousa, M. H. Elsayed, Y. Ye and S. W. Kuo, Tetraphenylanthraquinone and Dihydroxybenzene-Tethered Conjugated Microporous Polymer for Enhanced CO_2 Uptake and Supercapacitive Energy

Storage, *JACS Au*, 2024, **4**, 3593–3605, DOI: 10.1021/jacsau.4c00537.

29 J. S. M. Lee and A. I. Cooper, Advances in Conjugated Microporous Polymers, *Chem. Rev.*, 2020, **120**, 2171–2214, DOI: 10.1021/acs.chemrev.9b00399.

30 M. G. Mohamed, B. X. Su and S. W. Kuo, Robust Nitrogen-Doped Microporous Carbon via Crown Ether-Functionalized Benzoxazine-Linked Porous Organic Polymers for Enhanced CO_2 Adsorption and Supercapacitor Applications, *ACS Appl. Mater. Interfaces*, 2024, **16**, 40858–40872, DOI: 10.1021/acsami.4c05645.

31 M. G. Mohamed, M. H. Elsayed, C. J. Li, A. E. Hassan, I. M. A. Mekhemer, A. F. Musa, M. K. Hussien, L. C. Chen, K. H. Chen, H. Chou and S. W. Kuo, Reticular design and alkyne bridge engineering in donor–π–acceptor type conjugated microporous polymers for boosting photocatalytic hydrogen evolution, *J. Mater. Chem. A*, 2024, **12**, 7693–7710, DOI: 10.1039/D3TA07309B.

32 Y. Liao, H. Wang, M. Zhu and A. Thomas, Efficient supercapacitor energy storage using conjugated microporous polymer networks synthesized from Buchwald–Hartwig coupling, *Adv. Mater.*, 2018, **30**, 1705710, DOI: 10.1002/adma.201705710.

33 W. Zhang, H. Zuo, Z. Cheng, Y. Shi, Z. Guo, N. Meng, A. Thomas and Y. Liao, Macroscale conjugated microporous polymers: Controlling versatile functionalities over several dimensions, *Adv. Mater.*, 2022, **34**, 2104952, DOI: 10.1002/adma.202104952.

34 L. Chen, B. Chen, J. Kang, Z. Yan, Y. Jin, H. Yan, S. Chen and C. Xia, The synthesis of a novel conjugated microporous polymer and application on photocatalytic removal of uranium (VI) from wastewater under visible light, *Chem. Eng. J.*, 2022, **431**, 133222, DOI: 10.1016/j.cej.2021.133222.

35 M. Wu, Z. Shan, B. Xu and G. Zhang, Anion anchored conjugated microporous polymers as solid electrolytes, *Chem. Eng. J.*, 2022, **427**, 131728, DOI: 10.1016/j.cej.2021.131728.

36 A. Hayat, M. Sohail, A. El Jery, K. M. Al-Zaydi, S. Raza, H. Ali, Y. Al-Hadeethi, T. A. Taha, I. Ud Din, M. Ali Khan, M. A. Amin, E. Ghasali, Y. Orooji, Z. Ajmal and M. Z. Ansari, Recent advances in ground-breaking conjugated microporous polymers-based materials, their synthesis, modification and potential applications, *Mater. Today*, 2023, **64**, 180–208, DOI: 10.1016/j.mattod.2023.02.025.

37 X. Liu, C. F. Liu, S. Xu, T. Cheng, S. Wang, W. Y. Lai and W. Huang, Porous organic polymers for high-performance supercapacitors, *Chem. Soc. Rev.*, 2022, **51**, 3181–3225, DOI: 10.1039/D2CS00065B.

38 M. G. Mohamed, A. F. M. EL-Mahdy, M. G. Kotp and S. W. Kuo, Advances in porous organic polymers: Syntheses, structures, and diverse applications, *Mater. Mater. Adv.*, 2022, **3**, 707–733, DOI: 10.1039/D1MA00771H.

39 A. O. Mousa, Z. I. Lin, C. H. Chuang, C. K. Chen, S. W. Kuo and M. G. Mohamed, Rational design of bifunctional microporous organic polymers containing anthracene and triphenylamine units for energy storage and biological applications, *Int. J. Mol. Sci.*, 2023, **24**, 8966, DOI: 10.3390/ijms24108966.

40 M. M. Samy, I. M. A. Mekhemer, M. G. Mohamed, M. H. Elsayed, K. H. Lin, Y. K. Chen, T. L. Wu, H. H. Chou and S. W. Kuo, Conjugated microporous polymers incorporating Thiazolo [5,4-d] thiazole moieties for Sunlight-Driven hydrogen production from water, *Chem. Eng. J.*, 2022, **446**, 137158, DOI: 10.1016/j.cej.2022.137158.

41 M. G. Mohamed, S. U. Sharma, P. T. Wang, M. Ibrahim, M. H. Lin, C. L. Liu, M. Ejaz, H. J. Yen and S. W. Kuo, Construction of fully π-conjugated, diyne-linked conjugated microporous polymers based on tetraphenylethene and dibenzo[g,p]chrysene units for energy storage, *Polym. Chem.*, 2024, **15**, 2827–2839, DOI: 10.1039/D4PY00421C.

42 B. Luo, Y. Chen, Y. Zhang and J. Huo, Nitrogen-rich anthraquinone–triazine conjugated microporous polymer networks as high-performance supercapacitor, *New J. Chem.*, 2021, **45**, 17278–17286, DOI: 10.1039/D1NJ03180E.

43 S. U. Sharma, M. H. Elsayed, I. M. A. Mekhemer, T. S. Meng, H. H. Chou, S. W. Kuo and M. G. Mohamed, Rational design of pyrene and thienyltriazine-based conjugated microporous polymers for high-performance energy storage and visible-light photocatalytic hydrogen evolution from water, *Giant*, 2024, **17**, 100217, DOI: 10.1016/j.giant.2023.100217.

44 X. Gao, C. Shu, C. Zhang, W. Ma, S. B. Ren, F. Wang, Y. Chen, J. H. Zeng and J. X. Jiang, Substituent effect of conjugated microporous polymers on the photocatalytic hydrogen evolution activity, *J. Mater. Chem. A*, 2020, **8**, 2404–2411, DOI: 10.1039/C9TA13212K.

45 L. Chen, Y. Li, X. Wang, J. Wu, Y. Ding, S. B. Ren, L. Zhang, Z. Xu, B. Chen, D. M. Han and Y. P. Wu, Conjugated microporous polyimide cathodes for sodium/lithium-ion batteries with ultra-long cycling performance, *Chem. Eng. J.*, 2023, **464**, 142658, DOI: 10.1016/j.cej.2023.142658.

46 Z. Chen, Y. Wang, Z. Ning, Q. Huang, J. Zhou and F. Yu, Conjugated Microporous Polymer/TiS_2 Composite Cathode for High-Performance Lithium-Rechargeable Batteries, *ACS Appl. Polym. Mater.*, 2024, **6**, 13110–13119, DOI: 10.1021/acsapm.4c02203.

47 X. Wang, C. Zhang, Y. Xu, Q. He, P. Mu, Y. Chen, J. Zeng, F. Wang and J. X. Jiang, Conjugated Microporous Polytetra(2-Thienyl)ethylene as High Performance Anode Material for Lithium- and Sodium-Ion Batteries, *Macromol. Chem. Phys.*, 2018, **219**, 1700524, DOI: 10.1002/macp.201700524.

48 S. Zhang, W. Huang, P. Hu, C. Huang, C. Shang, C. Zhang, R. Yang and G. Cui, Conjugated microporous polymers with excellent electrochemical performance for lithium and sodium storage, *J. Mater. Chem. A*, 2015, **3**, 1896–1901, DOI: 10.1039/c4ta06058j.

49 H. Li, M. Tang, Y. Wu, Y. Chen, S. Zhu, B. Wang, C. Jiang, E. Wang and C. Wang, Large π-Conjugated Porous Frameworks as Cathodes for Sodium-Ion Batteries, *J. Phys. Chem. Lett.*, 2018, **9**, 3205–3211, DOI: 10.1021/acs.jpclett.8b01285.

50 T. Yang, C. Zhang, W. Ma, X. Gao, C. Yan, F. Wang and J. X. Jiang, Thiophene-rich conjugated microporous

polymers as anode materials for high performance lithium- and sodium-ion batteries, *Solid State Ion*, 2020, **347**, 115247, DOI: **10.1016/j.ssi.2020.115247**.

51 M. G. Mohamed, S. U. Sharma, C. H. Yang, M. M. Samy, A. K. K. Mohammed, S. V. Chaganti, J. T. Lee and S. W. Kuo, Anthraquinone-Enriched Conjugated Microporous Polymers as Organic Cathode Materials for High-Performance Lithium-Ion Batteries, *ACS Appl. Energy Mater.*, 2021, **4**, 14628–14639, DOI: **10.1021/acsaem.1c03270**.

52 Y. Xie and Z. Li, Recent advances in the Z/E isomers of tetraphenylethene derivatives: stereoselective synthesis, AIE mechanism, photophysical properties, and application as chemical probes, *Chem. Asian J.*, 2019, **14**, 2524–2541, DOI: **10.1002/asia.201900282**.

53 M. Fu, C. Zhang, Y. Chen, K. Fan, G. Zhang, J. Zou, Y. Gao, H. Dai, X. Wang and C. A. Wang, thianthrene-based small molecule as a high-potential cathode for lithium–organic batteries, *Chem. Commun.*, 2022, **58**, 11993–11996, DOI: **10.1039/D2CC04765A**.

54 A. Basit, M. G. Mohamed, S. U. Sharma and S. W. Kuo, Thianthrene-and Thianthrene Tetraoxide-Functionalized Conjugated Microporous Polymers for Efficient Energy Storage, *ACS Appl. Polym. Mater.*, 2024, **6**, 12247–12260, DOI: **10.1021/acsapm.4c02368**.

55 M. G. Mohamed, S. Y. Chang, M. Ejaz, M. M. Samy, A. O. Mousa and S. W. Kuo, Design and Synthesis of Bisulfone-Linked Two-Dimensional Conjugated Microporous Polymers for CO_2 Adsorption and Energy Storage, *Molecules*, 2023, **28**, 3234, DOI: **10.3390/molecules28073234**.

56 M. G. Mohamed, W. C. Chang and S. W. Kuo, Crown Ether- and Benzoxazine-Linked Porous Organic Polymers Displaying Enhanced Metal Ion and CO_2 Capture through Solid-State Chemical Transformation, *Macromolecules*, 2022, **55**, 7879–7892, DOI: **10.1021/acs.macromol.2c01216**.

57 M. G. Mohamed, T. C. Chen and S. W. Kuo, Solid-State Chemical Transformations to Enhance Gas Capture in Benzoxazine-Linked Conjugated Microporous Polymers, *Macromolecules*, 2021, **54**, 5866–5877, DOI: **10.1021/acs.macromol.1c00736**.

58 R. Mogensen, D. Brandell and R. Younesi, Solubility of the Solid Electrolyte Interphase (SEI) in Sodium Ion Batteries, *ACS Energy Lett.*, 2016, **1**, 1173–1178, DOI: **10.1021/acsenergylett.6b00491**.

59 F. Huang, P. Xu, G. Fang and S. Liang, In-Depth Understanding of Interfacial Na^+ Behaviors in Sodium Metal Anode: Migration, Desolvation, and Deposition, *Adv. Mater.*, 2024, **36**, 2405310, DOI: **10.1002/adma.202405310**.

60 J. Xu, M. Wang, N. P. Wickramaratne, M. Jaroniec, S. Dou and L. Dai, High-Performance Sodium Ion Batteries Based on a 3D Anode from Nitrogen-Doped Graphene Foams, *Adv. Mater.*, 2015, **27**, 2042–2048, DOI: **10.1002/adma.201405370**.

61 F. Lu, Y. Che, H. Tian, Y. Cai, Q. Kong, X. Yao and Z. Su, Anthraquinone-Based Conjugated Microporous Polymer as Anode for Long-Life Lithium Batteries, *ACS Appl. Polym. Mater.*, 2024, **6**, 15114–15123, DOI: **10.1021/acsapm.4c02652**.

62 X. Zhang, G. Zhu, M. Wang, J. Li, T. Lu and L. Pan, Covalent-organic-frameworks derived N-doped porous carbon materials as anode for superior long-life cycling lithium and sodium ion batteries, *Carbon*, 2017, **116**, 686–694, DOI: **10.1016/j.carbon.2017.02.057**.

63 M. S. Kim, W. J. Lee, S. M. Paek and J. K. Park, Covalent Organic Nanosheets as Effective Sodium-Ion Storage Materials, *ACS Appl. Mater. Interfaces.*, 2018, **10**, 32102–32111, DOI: **10.1021/acsami.8b09546**.

64 L. Shu, J. Yu, Y. Cui, Y. Ma, Y. Li, B. Gao and H. Wang, Porphyrin-based conjugated microporous polymers with dual active sites as anode materials for lithium-organic batteries, *Int. J. Hydrogen Energy*, 2022, **47**, 10902–10910, DOI: **10.1016/j.ijhydene.2022.01.146**.

65 S. Kim, M. Hankel, W. Cha, G. Singh, J. M. Lee, I. Y. Kim and A. Vinu, Theoretical and experimental investigations of mesoporous C_3N_5/MoS_2 hybrid for lithium and sodium ion batteries, *Nano Energy*, 2020, **72**, 104702, DOI: **10.1016/j.nanoen.2020.104702**.

66 K. Kannadasan, M. Govindasamy, C. Y. Kuo and P. Elumalai, Enhanced Lithium-ion/Sodium-ion Battery Performances Using Chrysanthemum Flower-like NiO-CoO Anode: Insights into Li^+/Na^+ Charge Storage Mechanism, *Electrochim. Acta*, 2025, **513**, 145574, DOI: **10.1016/j.electacta.2024.145574**.

67 Z. Zeng, B. A. Mei, G. Song, M. Hamza, Z. Yan, Q. Wei, H. Feng, Z. Zuo, B. Jia and R. Xiong, Physical interpretation of the electrochemical impedance spectroscopy (EIS) characteristics for diffusion-controlled intercalation and surface-redox charge storage behaviors, *J. Energy Storage*, 2024, **102**, 114021, DOI: **10.1016/j.est.2024.114021**.

68 M. Chandra, T. S. Khan, R. Shukla, S. Ahamad, A. Gupta, S. Basu, M. A. Haider and R. S. Dhaka, Diffusion coefficient and electrochemical performance of $NaVO_3$ anode in Li/Na batteries, *Electrochim. Acta*, 2020, **331**, 135293, DOI: **10.1016/j.electacta.2019.135293**.

69 J. Wang, E. Pameté, S. Yan, W. Zhao, J. Zhang, X. He, Z. Supiyeva, Q. Abbas and X. Pan, Sodium-ion diffusion coefficients in tin phosphide determined with advanced electrochemical techniques, *Electrochem. Commun.*, 2023, **150**, 107488, DOI: **10.1016/j.elecom.2023.107488**.

70 S. Grimme, J. Antony, S. Ehrlich and H. J. Krieg, A consistent and accurate ab initio parametrization of density functional dispersion correction (DFT-D) for the 94 elements H-Pu, *Chem. Phys.*, 2010, **132**, 154104, DOI: **10.1063/1.3382344**.

71 A. D. Becke and E. R. Johnson, Exchange-hole dipole moment and the dispersion interaction revisited, *J. Chem. Phys.*, 2007, **127**, 154108, DOI: **10.1063/1.2795701**.

72 A. S. G. El-hak, A. A. K. Mohammed, A. F. A. Hakiem and R. M. Mahfouz, Molecular conformation, vibrational spectroscopic and NBO analysis of atenolol and atenolol-hydrochlorothiazide cocrystals, *Spectrochim. Acta, Part A*, 2019, **222**, 117200, DOI: **10.1016/j.saa.2019.117200**.